applied optics

High brightness, low coherence, digital holographic microscopy for 3D visualization of an *in-vitro* sandwiched biological sample

D. G. Abdelsalam[1,*] and Takeshi Yasui[2,3]

[1]Engineering and Surface Metrology Lab, National Institute of Standards, Tersa St., El Haram, El Giza, Egypt
[2]Graduate School of Science and Technology, Tokushima University, 2-1, Minami-Josanjima, Tokushima 770-8506, Japan
[3]JST, ERATO, MINOSHIMA Intelligent Optical Synthesizer Project, 2-1, Minami-Josanjima, Tokushima 770-8506, Japan
*Corresponding author: dahi.abdelsalam@nis.sci.eg

Received 28 October 2016; revised 20 December 2016; accepted 20 December 2016; posted 21 December 2016 (Doc. ID 279673); published 26 January 2017

We achieve practically a bright-field digital holographic microscopy (DHM) configuration free from coherent noise for three-dimensional (3D) visualization of an *in-vitro* sandwiched sarcomere sample. Visualization of such sandwiched samples by conventional atomic force microscope (AFM) is impossible, while visualization using DHM with long coherent lengths is challenging. The proposed configuration is comprised of an ultrashort pulse laser source and a Mach–Zehnder interferometer in transmission. Periodically poled lithium niobate (PPLN) crystal was used to convert the fundamental beam by second harmonic generation (SHG) to the generated beam fit to the CCD camera used. The experimental results show that the contrast of the reconstructed phase image is improved to a higher degree compared to a He–Ne laser based result. We attribute this improvement to two things: the feature of the femtosecond pulse light, which acts as a chopper for coherent noise suppression, and the fact that the variance of a coherent mode can be reduced by a factor of 9 due to low loss through a nonlinear medium.

OCIS codes: (070.6110) Spatial filtering; (090.1995) Digital holography; (100.5090) Phase-only filters; (170.0180) Microscopy.

https://doi.org/10.1364/AO.56.0000F1

1. INTRODUCTION

The study of coherent noise suppression in digital holographic microscopy (DHM) is an important matter in the fields of both engineering and biological science [1]. DHM enables the extraction of both intensity and phase information of a wave diffracted by a specimen from a single hologram with high resolution [2,3]. In usual DHM, optical sources with long coherent lengths such as a He–Ne laser have been widely used to feature the non-sandwiched biological specimens. Because of the high degree of coherence of the He–Ne laser light, harmful coherent noise often appears [4–6]. This noise influences the quality of the holograms and a subsequent error in phase measurement is produced. The bigger the phase noise, the less accurate the measurement will be. The harmful coherent noise is mainly produced from two sources. The first is the random diffraction patterns (speckle noise), which is attributed to the scattered light. The second is the formation of undesirable interference fringes (spurious noise) due to stray light. The spurious noise is formed when light reflected or scattered from various surfaces in the optical path is coherent with the original beam. The amplitude of the scattered light $\mathbf{a}_s$ combines vectorially to the amplitude $\mathbf{a}$ of the original beam, resulting in a phase error $\Delta\varphi$, as illustrated in Fig. 1(a) [7,8]. The phase φ is given by $(2\pi/X)$, X being the extra path traversed by the stray light. In the case of sandwiched samples, where the sample is inserted in between two thin glass plates to avoid dehydration, the phase error $\Delta\varphi$ is considerable. Some practical solutions such as introducing a wedged beam splitter, a rotating diffuser, and anti-reflection coating to the optical component surfaces in the optical system setup were proposed to reduce this phase error [8]. Although these practical solutions are effective and may reduce the coherent noise, they have some demerits in terms of blurring the fringe visibility and hindering the fringe production in DHM, which requires perfect alignment. Numerical techniques have been proposed to suppress such coherent noise. Abdelsalam and Kim [9] used a numerical method based on flat fielding with apodized apertures to minimize the coherent noise in the phase-contrast image by an order of 65%. Although this numerical technique is effective in reducing such coherent noise in the reconstructed object-wave (amplitude and phase), it offers tradeoffs between the apodized aperture size and the quality of the formed noise level.

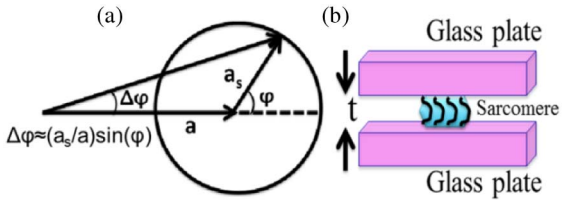

Fig. 1. (a) Phase error $\Delta\varphi$ (background spurious noise) created by scattered long coherent light $\mathbf{a}_s$, and (b) sliced biological sample mounted in between two thin glass plates to avoid dehydration.

Furthermore, that technique was applied for non-sandwiched samples. Optical sources with short coherent lengths such as LEDs were suggested to avoid the harmful coherent noise [10–12]. However, the limited coherence length of LED and its insufficient brightness hinders its application in an off-axis DHM, since just a limited number of interference fringes with low visibility appear in the field-of-view (FOV). Zhang *et al.* [13] used a wide-field microscope based on an in-line digital holography configuration with LEDs as optical sources for imaging non-sandwiched biological samples. Although the in-line configuration of holography can make full use of the resolving power of the camera used, it suffers from the existence of both zero order and twin image in the reconstructed object-wave. In contrast, using DHM with long coherent laser sources such as He–Ne to visualize the sandwiched biological samples is challenging because of the existence of the harmful coherent noise (speckle and spurious). It is worth mentioning that visualization of sandwiched biological samples is considered difficult to achieve by mechanical microscopes such as AFM. Therefore, in this paper, we present an off-axis DHM scheme using femtosecond pulse light with ultrashort coherent length, which makes it possible to visualize sandwiched samples with no spurious or speckle noises in the reconstructed object-wave. PPLN crystal was used to produce bright light by the SHG conversion process. We used the PPLN crystal for two reasons: to convert the fundamental beam of wavelength of 1550 nm into the generated beam of wavelength 777.8 nm fit to the camera used, and because the variance of the coherent mode of the fundamental beam can be reduced by a factor of 9 due to low loss through a nonlinear medium [14]. This generated bright light with a Mach–Zehnder interferometer in transmission is used to visualize a sandwiched microstructured sarcomere sample. The sarcomeres are isolated fibers dissected from rabbit muscle and mounted in between two thin glass plates (gap distance $t = 15$ μm) to avoid dehydration. A schematic diagram to place a fresh, sliced biological specimen in DHM is shown in Fig. 1(b).

2. EXPERIMENTAL SETUP

The experimental setup consisted of two parts: generation of bright femtosecond pulse light in the near-infrared region and a Mach–Zehnder interferometer in transmission, as demonstrated in Fig. 2. A mode-locked Er-doped fiber laser light (center wavelength $\lambda_c = 1550$ nm, spectral bandwidth $\Delta\lambda = 73$ nm, pulse duration $\Delta\tau = 100$ fs, mean power $P_{\text{mean}} = 380$ mW, and repetition frequency $f_{\text{rep}} = 250$ MHz) was converged by

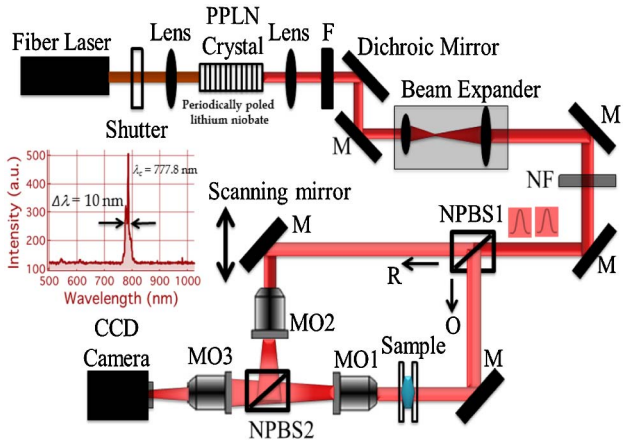

Fig. 2. Experimental setup. PPLN, periodically poled lithium niobate crystal; F, bandpass filter at 775 nm; M, mirror; NF, neutral density filter; NPBS1 and NPBS2, nonpolarizing beam splitters; MO1, MO2, and MO3, microscope objectives with (50×, NA = 0.45), (50×, NA = 0.45), and (20×, NA = 0.1), respectively.

a focusing lens on a periodically poled lithium niobate (PPLN) crystal to convert the wavelength by SHG into the operating wavelength region of a charged coupled device (CCD) camera. To generate the bright light by SHG process, we used a narrow bandpass optical filter with a specification of F, passband wavelength = 775 ± 5 nm. The generated bright light by SHG mechanism has λ_c of 777.8 nm, $\Delta\lambda$ of 10 nm, $\Delta\tau$ of 120 fs, and P_{mean} of 14 mW. The output power was sufficient to illuminate the sample and form off-axis holograms with high contrast in the entire field of the CCD camera. The coherence length of the generated bright pulse light by SHG process was measured to be 30 μm. The generated bright pulse light beam was enlarged to a diameter of 20 mm by a telescope system. This enlargement of the falling pulse beam is important to overcome the vignetting of the lenses used in the optical setup. In the Mach–Zehnder off-axis scheme in transmission, a pair of non-polarized beam splitters (NPBS1 and NPBS2) was used to divide the two SHG pulse beams into reference (R) and object (O) beams and combine them again at the plane of NPBS2. Disparity of optical path length in the two arms of the interferometer was precisely adjusted within the coherence length of 30 μm by a scanning mirror, equipped with a precise mechanical translation stage, in the reference arm of the interferometer. Note that the object that is a sandwiched microstructured sarcomere sample is positioned carefully in the object arm to check the region of interest first before capturing the off-axis hologram. The idea is to visualize the same region or an area very close to the region that is tested by phase contrast microscope. Photographs of the investigated sample taken by both the phase contrast microscope and the proposed DHM with blocking the reference arm are shown in Figs. 3(a) and 3(b), respectively. The number of sarcomeres in Fig. 3(a) is 25, while the number of sarcomeres in Fig. 3(b) is 30. The difference in the number of sarcomeres is due to the difference in magnification. Testing sarcomere length and thickness has an important determinant and indicator of cardiac mechanical function [15]. To test the thickness of the sarcomeres, off-axis fringes should be formed to cover the region

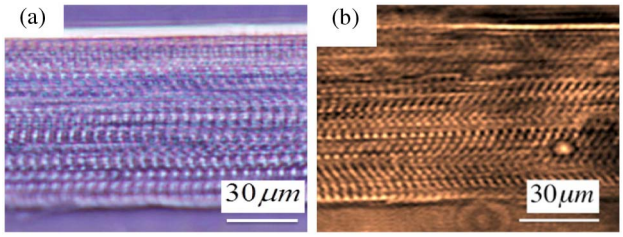

Fig. 3. Photographs of the investigated sarcomere sample (a) taken by phase contrast microscope, and (b) taken by the proposed optical setup with blocking of the reference arm.

of interest shown in Fig. 3(b). Off-axis fringes are formed when the interference of the object and the reference beams are tilted at a small angle with respect to each other. The off-axis hologram is formed at the plane of the beam splitter NPBS2. The off-axis hologram was recorded by making the reference wave (instead of the object wave) subtending the off-axis angle with the optical axis. Such arrangement is not only easier to align, but also makes the image plane parallel to the sensor surface. The formed off-axis hologram was transferred to a black-and-white CCD camera (640 pixel by 480 pixel, pixel size = 4.3 μm) using a microscope lens MO3 (20×, NA = 0.1).

3. RECONSTRUCTION METHOD

The light coming from the beam expander is assumed to be an ideal plane wave. The microscopic objective (MO2) should be identical to the microscopic objective (MO1) to cancel out the net sphericity and maintain the ideality of the plane wave. As shown in Fig. 4, the object wave O propoagates along $0z$ direction with normal incidence on the CCD plane $0xy$. The reference wave R propagates with an angle respect to the $0z$. The off-axis digital hologram intensity $I(k, l)$ recorded by the CCD camera can be written by the following expression [16]:

$$I(k, l) = |O|^2 + |R|^2 + R^*O + RO^*, \quad (1)$$

where k, l are discrete coordinates in the hologram plane and $*$ stands for the complex conjugate *and*. In Eq. (1), the first two intensity terms are of zero order, which can be directly filtered in the Fourier domain [17,18], and the last two are the interference terms.

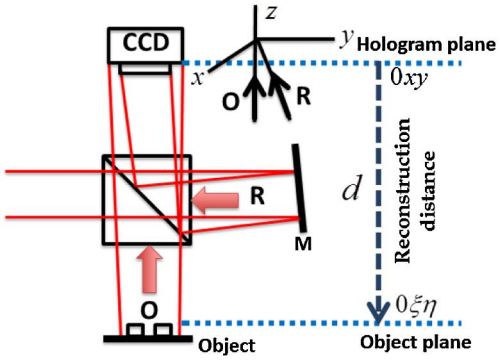

Fig. 4. Off-axis geometry at the incidence on the CCD camera. The 0xy plane is parallel to the CCD camera.

The reconstructed wave front ψ of the recorded hologram in the observation plane $0\xi\eta$ has been obtained by computing the Fresnel integral of the digitized hologram $I(k, l)$ and is given by [16]

$$\psi(\mathrm{m}, \mathrm{n}) = A \exp\left[\frac{\mathrm{i}\pi}{\lambda \mathrm{d}}(m^2\Delta\xi^2 + n^2\Delta\eta^2)\right] \times \mathrm{FFT}\left\{R_D(k, l)I(k, l) \times \exp\left[\frac{\mathrm{i}\pi}{\lambda \mathrm{d}}(k^2\Delta x^2 + l^2\Delta y^2)\right]\right\}_{\mathrm{m,n}}, \quad (2)$$

where m, n, k, and l are integers and λ is the wavelength of the laser light. A is a complex constant given as $A = \exp(i2\pi/\lambda)/(i\pi\lambda)$, and FFT denotes a two-dimensional (2D) fast Fourier transform. Δx and Δy refer to the sampling intervals in the hologram plane. The digital reference wave $R_D(m, n)$ is defined as $R_D(m, n) = A_R \exp[i(2\pi/\lambda)(k_x m\Delta x + k_y n\Delta y)]$. The sampling intervals $\Delta\xi$ and $\Delta\eta$ in the observation plane are related to size of the CCD (L) and to the distance d as $\Delta\xi = \Delta\eta = \lambda d/L$. After the FFT of the hologram is computed, three spectra are obtained. One specrum is selected by applying a spatial filtering technique and the inverse FFT is computed. The amplitude-contrast image can be obtained by using the following intensity $[\mathrm{Re}(\psi(m, n))^2 + \mathrm{Im}(\psi(m, n))^2]$ and the phase-contrast image can be obtained by the argument $\arctan[\mathrm{Re}(\psi(m, n))/\mathrm{Im}(\psi(m, n))]$. To reconstruct the object-wave in the observation plane, the two components of the wave vectors k_x and k_y are adjusted such that the propagation direction of $R_D(m, n)$ coincides as closely as possible with that of the experimental reference wave.

4. EXPERIMENTAL RESULTS AND DISCUSSION

Figures 5(a) and 5(b) show the off-axis holograms of the sarcomere sample obtained by a He–Ne laser light with wavelength 632.8 nm and femtosecond pulse light with wavelength 777.8 nm, respectively. Note that the off-axis hologram demonstrated in Fig. 5(a) was produced by the same experimental setup shown in Fig. 2 by replacing the femtosecond pulse light with a He–Ne laser light. A layered structure of around 15 sarcomeres was captured at nearly the same region of FOV. Comparison of these images indicated that the image brightness of DHM with the femtosecond pulse light was higher than that with the He–Ne laser light due to temporally localized energy of the femtosecond pulse light. Figures 6(a) and 6(b) show one filtered spectrum $\Psi = R^*O$ from the three spectra in 2D-FFT of Figs. 5(a) and 5(b), respectively.

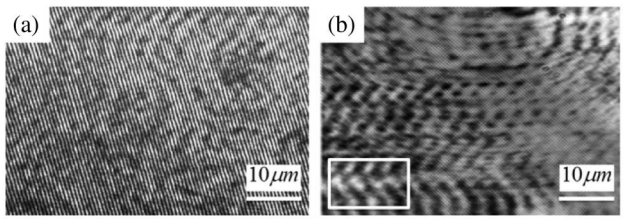

Fig. 5. Off-axis holograms of layered structure of sarcomeres taken by (a) He–Ne laser light, and (b) femtosecond pulse light.

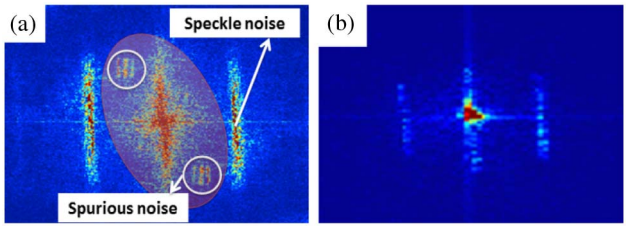

Fig. 6. Filtered 2D-FFT spectrum of off-axis holograms of the sarcomere sample with (a) He–Ne laser light, and (b) femtosecond pulse light.

Note that the three spectra appear in the filtered one spectrum are attributed to the off-axis fringes of the sarcomere sample itself. The spurious and speckle noises are clearly observed in the frequency domain of Fig. 6(a), while such noise completely disappeared when we used our setup, which is shown in Fig. 6(b).

Figure 7 shows the sequential reconstruction steps of the off-axis hologram with femtosecond pulse light. The reconstructed amplitude and phase was recorded by selecting the appropriate values of the two components of the wave vector $k_x = 0.00999\ \text{mm}^{-1}$ and $k_y = -0.5239\ \text{mm}^{-1}$ for the off-axis hologram with He–Ne laser and $k_x = 0.02145\ \text{mm}^{-1}$ and $k_y = -0.51570\ \text{mm}^{-1}$ for that with the femtosecond pulse light.

To see the effectiveness of our setup compared to the conventional DHM with He–Ne laser light, we have not applied any of the numerous image enhancement techniques [19,20] to significantly improve the perceived image quality for biological applications. Figures 8(a) and 8(b) show the reconstructed 3D pseudocolor amplitude map of Figs. 5(a) and 5(b), respectively. It is noted that these 3D reconstructed amplitude maps were flipped upside down to see the sarcomeres from a different side. In Fig. 8(a), the existence of spurious noise in the background image [see Fig. 5(a)] makes it difficult to visualize the structure

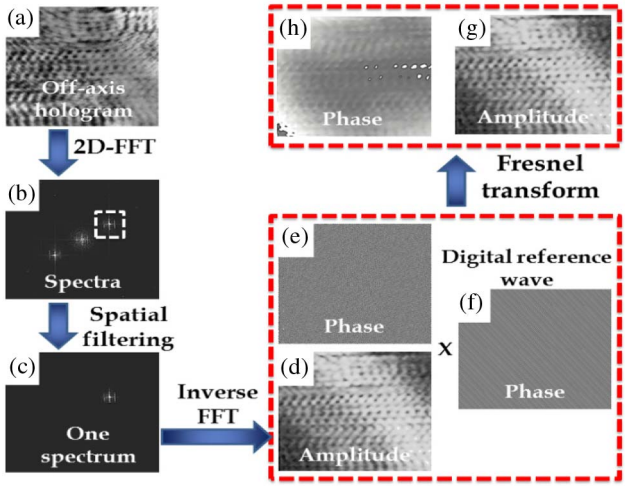

Fig. 7. Steps of reconstruction: (a) off-axis hologram obtained by femtosecond pulse light, (b) Fourier transformed spatial frequency domain spectra, (c) filtered one spectrum, (d, e) reconstructed amplitude- and phase-contrast images after computing the inverse FFT of the filtered spectrum, (f) simulated digital reference wave, and (g, h) final amplitude- and phase-contrast images.

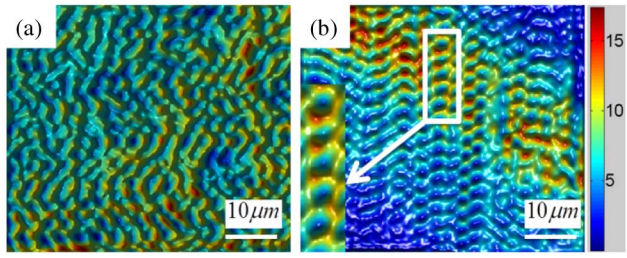

Fig. 8. 3D pseudocolor reconstructed amplitude-contrast image of (a) He–Ne laser light, and (b) femtosecond pulse light.

of the sarcomeres clearly. On the other hand, Fig. 8(b) shows the high quality and contrast of the structure detail on the sarcomeres, and provides accurate profile edges of the hexagonal shape of the sarcomeres. We believe these results show that our proposed technique is effective and preferable in featuring the sandwiched biological samples.

Our deductions were verified by applications of the apodization technique [21] to evaluate the coherent noise level in the off-axis holograms of Figs. 5(a) and 5(b). Apodization is the same topic as windowing in signal processing. The transmission of the apodized aperture function is perfectly transparent in the large central part of the profile. At the edges, the transmission varies from zero to unity following a curve defined by a cubic spline interpolation. A 2D transmission window that is 480 × 480 pixels and shown in Fig. 9(a) is multiplied with the off-axis holograms in Figs. 5(a) and 5(b), respectively. Note that the strong profile shape of the apodized function used approaches the triangle shape to clearly discriminate the intensity level at the middle of the image (small area occupies around four sarcomeres). Normalization of intensities distribution of four sarcomeres at the middle of the off-axis holograms in Figs. 5(a) and 5(b) before and after application of apodization are shown in Figs. 9(b) and 9(c), respectively.

As seen from Fig. 9(b), the variation in intensities before and after the application of apodization is considerable. This indicates that there is coherent noise in the reconstructed object wave (amplitude and phase). Such coherent noise totally disappears in Fig. 9(c), whereas there is no variation in the intensities distribution before and after the application of apodization. This validates our deductions that the reconstructed object wave created by the proposed technique is free from coherent noise and this technique is preferable to investigate sandwiched biological samples. Because of the low coherence bright pulse light used, the proposed technique

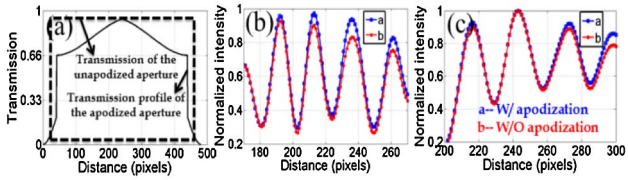

Fig. 9. Coherent noise estimation by apodization: (a) 2D transmission function, (b) 2D intensity distribution with and without apodization at the middle of Fig. 5(a), and (c) 2D intensity distribution with and without apodization at the middle of Fig. 5(b).

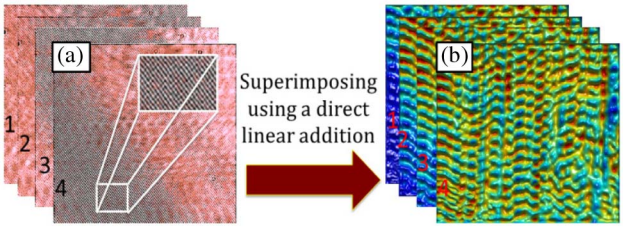

Fig. 10. Synthesized image (a) generated four off-axis holograms, and (b) synthesized reconstructed amplitude-contrast image.

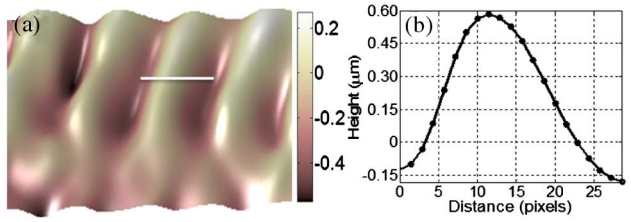

Fig. 12. (a) 3D height map converted from the reconstructed phase of the white rectangular area of Fig. 5(b) after removing the zero order by subtractions among the successive four holograms in Fig. 10(a), and (b) 2D phase profile along the white line of (a).

may suffer from a limited field of view. In this paper, we obtained full-field image by applying the synthesis image technique, which is used to superimpose many reconstructions from many off-axis holograms by a direct linear addition. Figure 10(a) shows four off-axis holograms generated by varying the optical path length of the interferometer. The gray regions demonstrate high-contrast fringes, while the non-gray regions demonstrate low-contrast fringes. The full field synthesized amplitude contrast-image shown in Fig. 10(b) was obtained by adding the reconstruction of the amplitude-contrast image of each off-axis hologram of Fig. 10(a).

Because phase images tend to suffer from coherent noise to a significantly less degree compared to the amplitude images, the results of phase distributions reconstructed from Figs. 5(a) and 5(b) were converted to height distributions [22] and compared. Figures 11(a) and 11(b) show 3D pseudocolor height distribution images of the stripe structures of 10 sarcomeres of Figs. 5(a) and 5(b), respectively. As seen in Fig. 11(a), the sarcomeres are hardly viewed in Fig. 11(a) because of the existence of coherent noise in the background. In contrast, Fig. 11(b) shows that the stripe structures of the sarcomeres are clearly viewed because there is no coherent noise in the background image. The 2D height profile extracted along the red and blue lines in Figs. 11(a) and 11(b) are shown in Fig. 11(c), indicating the cross-sectional profile of one sarcomere.

The height profile extracted by the proposed technique was estimated to be 0.72 μm along one sarcomere [blue line in Fig. 11(c)]. On the other hand, the height profile extracted along one sarcomere [red line in Fig. 11(c)] was estimated to be 0.53 μm. We believe that the estimated height may be varied from one sarcomere to the other, so many sarcomeres

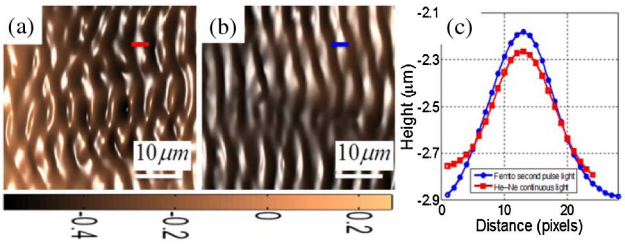

Fig. 11. 3D pseudocolor height map converted from the reconstructed phase-contrast image of stripy sarcomere with (a) He–Ne laser light, (b) femtosecond pulse light, and (c) 2D height profiles along the red and blue lines in (a) and (b).

were measured at different positions and the ratio is still considerable. We attribute this phase difference to the coherent noise (speckle and spurious) and the instability of He–Ne laser light. It is due to the fact that stray light or reflected ambient light (spurious noise from He–Ne) generally causes a reduction of contrast [23], as shown in Fig. 11(a). From these results, it could be said that the proposed technique is free from noise and the sarcomere cross-section can be calculated precisely with no need for time-consuming image enhancement techniques. A further improvement in contrast was applied to the proposed technique by removing the zero order of the synthesized hologram [24] produced from the four holograms shown in Fig. 10(a). Because of the holograms' shifting process, the reference and object beam may have some phase shifts. When the second hologram in Fig. 10 is subtracted from the first hologram, the zero order is removed. The subtraction process was done for the third to the second and the fourth to the third. Subtractions among the successive four holograms of Fig. 10(a) were superimposed using a direct linear addition method to form a high-quality synthesized hologram. The synthesized hologram was reconstructed by the same procedures demonstrated in Fig. 7 with no zero order in the frequency domain. Figure 12 shows the 3D pseudocolor height map converted from the reconstructed phase of the white rectangular of Fig. 5(b) after removing the zero order by subtractions among the successive four holograms in Fig. 10(a). The height profile extracted along the white line in Fig. 12(a) is shown in Fig. 12(b), indicating the cross-sectional height profile of one sarcomere and estimated to be 0.74 μm. As seen from Fig. 12, the contrast is improved and we attribute this improvement to the zero order elimination in addition to any random noise during the scanning process. The average thickness measurement of the sarcomere is approximately consistent with the results published in [25].

The repeatability of the optical setup, which is defined as the root mean square (RMS) of the height difference for two measurements on the sample-free setup, is around 10 nm. We believe that the repeatability of the setup can be further improved by lessening the exposure time of the CCD camera used, in addition to reducing the environmental disturbance.

5. CONCLUSION

In this paper, we presented the use of the femtosecond laser bright light in a Mach–Zehnder interferometer to enhance the image contrast while suppressing the coherent noise in

DHM. The presented method was effectively applied to investigate the structure of a sarcomere sample mounted between two thin glass plates. Compared to the DHM with long coherent He–Ne laser light, the proposed setup is insensitive to coherent noise. This insensitivity to coherent noise can be attributed to the features of the femtosecond pulse light with an ultrashort coherent length, as well as the high brightness light generated by the nonlinear system, which reduces the coherent mode of the fundamental light by a factor of 9. Further improvement in contrast was achieved by applying the synthesis image technique. The proposed technique can provide a fast inspection of the uniformity of 3D nanopatterns as well as enhanced image contrast with no need for image enhancement techniques for coherent noise suppression.

Funding. Japan Science and Technology Agency (JST), Exploratory Research for Advanced Technology, MINOSHIMA Intelligent Optical Synthesizer Project; Ministry of Education, Culture, Sports, Science, and Technology of Japan (Grants-in-Aid for Scientific Research No. 26246031).

REFERENCES

1. M. Born and E. Wolf, *Principles of Optics* (Cambridge University, 1980).
2. D. G. Abdelsalam and D. Kim, "Two-wavelength in-line phase-shifting interferometry based on polarizing separation for accurate surface profiling," Appl. Opt. **50**, 6153–6161 (2011).
3. M. K. Kim, *Digital Holographic Microscopy: Principles, Techniques, and Applications* (Springer-Verlag, 2011).
4. O. Kwon, J. C. Wyant, and C. R. Hayslett, "Rough surface interferometry at 10.6 μm," Appl. Opt. **19**, 1862–1869 (1980).
5. F. Pan, W. Xiao, S. Liu, and L. Rong, "Coherent noise reduction in digital holographic phase contrast microscopy by slightly shifting object," Opt. Express **19**, 3862–3869 (2011).
6. C. Liu and M. K. Kim, "Digital holographic adaptive optics for ocular imaging: proof of principle," Opt. Lett. **36**, 2710–2712 (2011).
7. C. J. Kuo and M. H. Tsai, *Three-Dimensional Holographic Imaging* (Wiley, 2002).
8. P. Hariharan, *Basics of Interferometry* (1991).
9. D. G. Abdelsalam and D. Kim, "Coherent noise suppression in digital holography based on flat fielding with apodized apertures," Opt. Express **19**, 17951–17959 (2011).
10. F. Dubois, L. Joannes, and J. Legros, "Improved three-dimensional imaging with a digital holography microscope with a source of partial spatial coherence," Appl. Opt. **38**, 7085–7094 (1999).
11. B. Kemper, S. Sturwald, C. Remmersmann, P. Langehanenberg, and G. von Bally, "Characterisation of light emitting diodes (LEDs) for application in digital holographic microscopy for inspection of micro and nanostructured surfaces," Opt. Lasers Eng. **46**, 499–507 (2008).
12. O. Mudanyali, E. McLeod, W. Luo, A. Greenbaum, A. F. Coskun, Y. Hennequin, C. P. Allier, and A. Ozcan, "Wide-field optical detection of nanoparticles using on-chip microscopy and self-assembled nanolenses," Nat. Photonics **7**, 240–247 (2013).
13. Y. Zhang, A. Greenbaum, W. Luo, and A. Ozcan, "Wide-field pathology imaging using on-chip microscopy," Virchows Arch. **467**, 3–7 (2015).
14. M. T. Simons and I. Novikova, "Bright squeezed light via second harmonic generation in a whispering-gallery mode resonator" (College of William & Mary).
15. G. Bub, P. Camelliti, C. Bollensdorff, D. J. Stuckey, G. Picton, R. A. B. Burton, K. Clarke, and P. Kohl, "Measurement and analysis of sarcomere length in rat cardiomyocytes in situ and in vitro," Am. J. Physiol. Heart Circ. Physiol. **298**, H1616–H1625 (2010).
16. T. Colomb, P. Dahlgren, D. Beghuin, E. Cuche, P. Marquet, and C. Depeursinge, "Polarization imaging by use of digital holography," Appl. Opt. **41**, 27–37 (2002).
17. E. Cuche, P. Marquet, and C. Depeursinge, "Spatial filtering for zero-order and twin-image elimination in digital off-axis holography," Appl. Opt. **39**, 4070–4075 (2000).
18. E. Cuche, F. Bevilacqua, and C. Depeursinge, "Digital holography for quantitative phase-contrast imaging," Opt. Lett. **24**, 291–293 (1999).
19. D. G. Abdelsalam, M. S. Shaalan, and M. M. Eloker, "Surface microtopography measurement of a standard flat surface by multiple-beam interference fringes at reflection," Opt. Lasers Eng. **48**, 543–547 (2010).
20. D. G. Abdelsalam, M. S. Shaalan, M. M. Eloker, and D. Kim, "Radius of curvature measurement of spherical smooth surfaces by multiple-beam interferometry in reflection," Opt. Lasers Eng. **48**, 643–649 (2010).
21. D. G. Abdelsalam, J. Min, D. Kim, and B. Yao, "Digital holographic shape measurement using Fizeau microscopy," Chin. Opt. Lett. **13**, 100701 (2015).
22. C. Zhang, P. S. Huang, and F.-P. Chiang, "Microscopic phase-shifting profilometry based on digital micromirror device technology," Appl. Opt. **41**, 5896–5904 (2002).
23. P. G. J. Barten, *Contrast Sensitivity of the Human Eye and Its Effects on Image Quality* (SPIE, 1999).
24. C. Liu, X. Yu, J. Hong, and M. K. Kim, "Image synthesis for off axis low coherence digital holography," in *Frontiers in Optics 2013/Laser Science* (OSA, 2013), paper JW3A.17.
25. I. Torre, A. G. Tendero, P. G. Canadilla, F. Crispi, F. G. Garcia, B. Bijnens, I. Iruretagoyena, J. Dopazo, I. A. Roldan, and E. Gratacos, "Permanent cardiac sarcomere changes in a rabbit model of intrauterine growth restriction," PLoS ONE **9**, e113067 (2014).